

## Radio frequency resonance measurements of the Ba $6sng$ - $6snh$ - $6sni$ - $6snk$ intervals: An investigation of the nonadiabatic effects in core polarization

T. F. Gallagher, R. Kachru, and N. H. Tran

*Molecular Physics Laboratory, SRI International, Menlo Park, California 94025*

(Received 17 May 1982)

Using a delayed field ionization approach we have observed the radio frequency resonance transitions connecting the Ba  $6sng$ ,  $6snh$ ,  $6sni$ , and  $6snk$  states for  $n \sim 20$ . The  $\Delta l$  intervals may be used to determine the dipole and quadrupole polarizabilities  $\alpha_d$  and  $\alpha_q$  of the  $Ba^+$  core with the use of both the familiar adiabatic core polarization model of Mayer and Mayer and a simple two-electron model of Van Vleck and Whitelaw. While both models give reasonable values for the dipole polarizability, the adiabatic model gives an impossible negative quadrupole polarizability. The two-electron model, however, gives values in reasonable agreement with calculations based on the Coulomb approximation. The values we determine for  $\alpha_d$  and  $\alpha_q$  are  $125.5(10)a_0^3$  and  $2050(100)a_0^5$ , respectively. Finally, the fine-structure splittings of the levels are roughly one hundred times larger than the analogous He splittings.

### I. INTRODUCTION

The depression of the energies of high angular momentum states of multielectron atoms below the hydrogenic value  $-\frac{1}{2}n^2$  was shown by Mayer and Mayer<sup>1</sup> to be due to the polarization of the core by the outer valence electron. They pointed out that the depression  $W_{\text{pol}}$  could be represented by

$$W_{\text{pol}} = -\frac{1}{2}\alpha_d \langle 1/r^4 \rangle - \frac{1}{2}\alpha_q \langle 1/r^6 \rangle, \quad (1)$$

where  $\alpha_d$  and  $\alpha_q$  are the quadrupole and dipole polarizabilities and  $\langle 1/r^4 \rangle$  and  $\langle 1/r^6 \rangle$  are expectation values of the inverse fourth and sixth powers of the orbital radius of the valence electron. This model assumes that the valence electron is stationary with  $\langle 1/r^4 \rangle$  and  $\langle 1/r^6 \rangle$  giving the squares of the electric field and field gradient from the valence electron at the ionic core. While this is a good approximation if the core electrons are moving much faster than the valence electron this is not the case if the speeds are comparable. In practice, Eq. (1) has been found to work very well for alkali atoms in which the ionic core has a closed shell.<sup>2-5</sup> However, it is not expected to work very well for an alkaline-earth atom with an alkali-like core. In fact, alkaline-earth atoms probably afford the best testing ground for any theories regarding the "nonadiabatic" effects which occur when the motion of the valence electron is not negligibly slow compared to that of the core electrons. There are two reasons for this. First, the alkaline-earth ions are alkali-like and

their polarizabilities are thus easily calculated. Second, the excitation energies of the excited states of alkaline-earth ions are very low  $\sim 1$  eV as opposed to  $\sim 20$  eV for the alkali atoms. Thus, the nonadiabatic effects should be relatively large.

Almost coincident with the work of Mayer and Mayer, Van Vleck and Whitelaw<sup>6</sup> considered the case in which there are two valence electrons, i.e., alkaline-earth-like atoms in which the ionic core is alkali-like. They showed that by using a straightforward expression for the potential of the atom, including explicitly the interaction between the two valence electrons and the actual states of the atom, it was possible to derive an accurate expression for the polarization energy analogous to Eq. (1) which includes the nonadiabatic effects and is thus valid for an alkaline-earth atom. The expression reduces in the limiting case exemplified by the alkali atoms to Eq. (1). Unfortunately there have not been systematic studies of alkaline earth or similar spectra to provide a stringent test of the theory.

In this paper, we report the first measurements of several series of  $\Delta l$  intervals for high- $l$  states in an alkaline-earth atom although we note that similar measurements of several  $d$ - $f$  transitions have recently been carried out by Vaidyanathan and Shorer.<sup>7</sup> Specifically, we have observed the Ba  $6sng$ - $6snh$ - $6sni$ - $6snk$  intervals for  $18 \leq n \leq 23$  using a radio frequency resonance approach. An analysis of the observed intervals using Eq. (1) leads to a negative quadrupole polarizability of the  $Ba^+$   $6s$  state which is clearly impossible. However, using the method of Van Vleck and Whitelaw, which is briefly reviewed,

our data can be fit to give reasonable values for the dipole and quadrupole polarizabilities of  $\text{Ba}^+$ , both of which are easily calculated.

## II. EXPERIMENTAL APPROACH

In these radio frequency resonance experiments we have used the delayed field ionization (DFI) scheme first used by Safinya *et al.*<sup>5</sup> The method uses the difference in radiative decay rates as a means of discriminating between states. Let us consider as an illustrative example the observation of the transition from the  $\text{Ba } 6s20g$  state to the longer-lived  $6s20h$  state. Ba atoms in an effusive beam are excited to the  $\text{Ba } 6sng$  state by a laser-cascade scheme described below and shown in Fig. 1. A microwave field is applied for  $1 \mu\text{s}$  after the pulsed laser excitation to drive the  $6s20g$ - $6s20h$  transition and then turned off. Three or four  $6sng$  lifetimes later we apply an electric field pulse which ionizes all the Rydberg atoms present. When the microwave frequency is far away from the  $6s20g$ - $6s20h$  resonance, a negligible number of  $6s20g$  atoms live long enough to be ionized. However, when the microwave frequency is tuned to the resonance, many atoms are left in the longer-lived  $6s20h$  state when the microwave field is turned off, and as a result more atoms live long enough to be field ionized. Thus, as the microwave frequency is swept through the  $6s20g$ - $6s20h$  resonance, an increase in the number of ions detected is observed, as shown in Fig. 2.

In principle, using the lifetimes as the basis for discriminating between adjacent  $l$  states is attractive

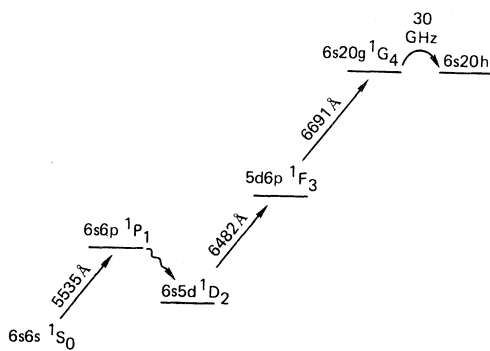


FIG. 1. Relevant energy levels for the study of the  $6s20g$ - $6s20h$  transitions. The three laser pumping steps are shown by the straight, nearly vertical arrows. The cascade from  $6s6p$  to  $6s5d$  is shown by the wavy arrow. The 30-GHz transition from  $6s20g$  to  $6s20h$  is shown by the curved arrow.

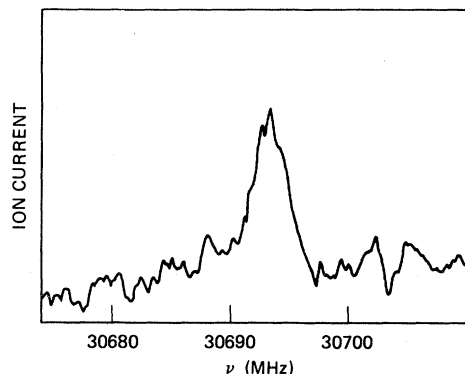


FIG. 2. A  $6s20g$ - $6s20h$  resonance on a sweep of increasing frequency.

because of its generality and the fact that no selectivity is required in the detection whether it be ionization or fluorescence detection. On the other hand, there are certain clear limitations. If the difference in the lifetimes is not large, long delay times are necessary which may lead to atoms passing out of the field of view and increased background signal due to black-body radiation induced transitions from the initially populated state to longer-living states.<sup>8</sup>

The atomic-beam apparatus is quite simple as shown by Fig. 3. An effusive beam of Ba is produced by a resistively heated oven and is collimated to a diameter of 3 mm about 5 cm from the oven. The atomic beam then passes between two plates which are 1 cm apart. A positive high-voltage pulse is applied to the lower plate to field ionize the atoms and accelerate the ions formed through a wire-mesh-covered aperture in the upper plate to an electron multiplier. The nearly collinear laser beams cross the atomic beam upstream of the aperture in the upper plate (see Fig. 3), how far depending on the delay before the application of the field ionization pulse.

The laser excitation scheme is shown in Fig. 1.

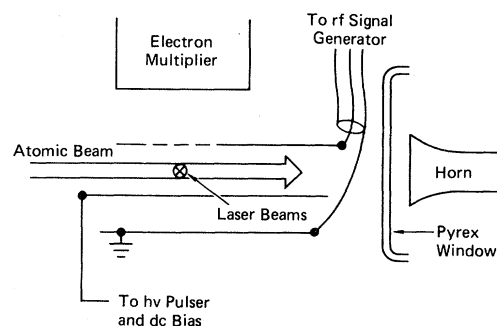


FIG. 3. Schematic diagram of the apparatus.

The first laser, at 5535 Å, excites the Ba atoms from the  $6s6s$  ground state to the  $6s6p$  state which decays in  $\sim 10$  ns. About 10% of the atoms excited to the  $6s6p$  state decay to the metastable  $6s5d$  state. To double the number of atoms in the  $6s5d$  state the 5535 Å laser beam is reflected back through the interaction region with an additional  $\sim 4$  m of optical path length, providing a delay of  $\sim 12$  ns. After a delay of 200 ns, the second laser beam, at 6482 Å, crosses the atomic beam exciting the  $6s5d$  atoms to the  $5d6p\ ^1F_3$  state. The third laser beam, tuned to the  $5d6p$ - $6sng$  transition at  $\sim 6700$  Å crosses the atomic beam about 5 ns after the second laser beam. Note that from the  $5d6p\ ^1F_3$  state it is possible to excite either  $6snd$  or  $6sng$  states; however, they may be easily distinguished using the polarizations of the lasers. If all the lasers are linearly polarized, either series can be excited; but, if all three lasers are circularly polarized the excitation of the  $6snd$  states is suppressed.

As shown by Fig. 3, the microwaves ( $\nu > 10$  GHz) are introduced through a reentrant Pyrex flange using a microwave horn. The radio frequency (rf) fields ( $\nu < 5$  GHz) are introduced by applying the rf voltage directly to the upper plate as shown by Fig. 3. The microwave source is a Hewlett-Packard 8690B sweep oscillator with backward wave oscillator plug-ins spanning the range from 12.4 to 40 GHz. Typical powers and bandwidths are 10 mW and 50 kHz. A critical feature of the experiment is the ability to turn off the microwave power completely 1  $\mu$ s after the laser excitation. This is done by applying a voltage pulse of  $-10$  V to the grid of the backward wave oscillator. The microwave power falls to less than 1% of its initial value in less than 10 ns and is left off for 50  $\mu$ s, a time longer than the duration of the experiment, but which allows the frequency of the oscillator to stabilize before the next shot of the laser 100 ms later. The rf oscillator, used in the  $g$ - $k$  transitions, is a Hewlett-Packard 8616A signal generator which has a power of 10 mW and frequency stability of  $\sim 50$  kHz. This signal generator is left on continuously, as the presence of the rf field alone does nothing to the  $6sng$  states.

As noted before, the rf power is applied directly to the upper plate of Fig. 3 through a 50  $\Omega$  coaxial cable. As the plates are a capacitor and do not even remotely resemble a 50  $\Omega$  load, the frequency response of the system is far from flat. Thus, there are sharp variations in the rf field between the plates as a function of rf frequency. In fact at some frequencies we are not able to detect any rf field between the plates. For this reason the rf frequency is

fixed and the microwave frequency is swept in the  $g$ - $k$  measurements.

The rf and microwave frequencies were measured with Hewlett-Packard 582 resonant cavity wave meters which were calibrated using a Hewlett-Packard 5340A microwave counter. This procedure was accurate to  $\pm 0.3$  MHz in the worst case ( $\nu \sim 40$  GHz). The microwave and rf power levels were recorded using a calibrated attenuator and detector, respectively.

### III. OBSERVATIONS

#### A. Preliminary observations

The choice of DFI as the detection technique is based upon several experimental observations. The most appealing method for rf resonance experiments in an atomic beam is selective field ionization (SFI), but we found that the field at which each Ba state ionizes is not sufficiently well defined to be useful. For example an increase from 10% to 90% of the maximum ionization signal of the Ba  $6s20g$  state requires a 20% change in the amplitude of the ionizing field pulse, and the difference in the field required for complete ionization of the  $6s19g$  and  $6s20g$  is only 20%. Thus, it is impossible to discriminate between  $6s20g$  and  $6s20h$  using field ionization. On the other hand measurements of the lifetimes of the  $6sng$  states made DFI appear more promising. For  $17 \leq n \leq 23$  we found lifetimes of  $\sim 5$   $\mu$ s, which are short enough that the atoms would clearly remain in a region where they could be detected for several  $6sng$  lifetimes.

Having decided to use DFI to observe the transitions, we were faced with the necessity of making a reasonable estimate of the transition frequencies. The optical measurements of Armstrong *et al.*<sup>9</sup> provide a starting point, as they give a quantum defect of 0.06 for the  $6sng\ 1G_4$  states which we are presumably exciting. This implies that the  $6s20g$  level lies  $\sim 50$  GHz below the hydrogenic  $n = 20$  level. If we make the assumption that this interval is entirely due to the dipole polarizability of  $Ba^+$  we estimate the Ba  $6s20g$ - $6s20h$  interval to be  $\sim 30$  GHz. To get another estimate for the  $g$ - $h$  interval, we swept the third laser in the vicinity of the  $n = 15$  and  $n = 16$   $6sng$  states while small,  $\sim 10$ – $50$  V/cm, electric fields were applied to enable us to observe the optical transitions to the  $6snh$  states which become allowed because of the  $g$  character admixed by the electric field. These observations suggested that the  $n = 15$  and  $n = 16$   $g$ - $h$  intervals were approximately 60 and 56 GHz and that the  $n = 20$   $g$ - $h$

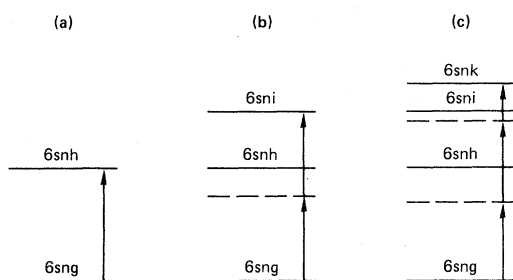


FIG. 4. The levels in the (a) one-photon  $6sng-6snh$  transitions, (b) the two-photon  $6sng-6sni$  transition, and (c) the three-photon  $6sng-6snk$  transitions. The virtual levels in (b) and (c) are shown by broken lines. In (c) the case in which the rf photon frequency is greater than the  $6sni-6snk$  interval is shown.

separation ought to be 33 GHz. Armed with these estimates we searched for the  $g-h$  resonances which could be power broadened to  $\sim 400$  MHz with our available powers,  $\sim 10$  mW. Note that the difference in the lifetimes of the  $g$  and  $h$  states is smaller than the corresponding difference for the  $g$  and  $i$  states, for example, so the signal-to-noise ratio is expected to be worse. However, since we were not sure where the transitions were, being able to power broaden the resonances seemed to be a significant advantage, and we searched for the  $g-h$  resonances first.

### B. Observed radio frequency transitions

We observed three types of transitions which are indicated schematically in Fig. 4. Both the one-photon  $g-h$  transitions and the two-photon  $g-i$  tran-

TABLE I.  $ng-nh$  frequencies.

$n$	Frequency (MHz)
18	40 179.2(12)
	41 146.6(22)
19	34 461.3(8)
	35 297.0(15)
20	30 011.9(7)
	30 692.5(10)
21	26 575.5(11)
	27 156.0(10)
22	24 241.5(10)
	24 746.8(4)
23	23 945.0(9) <sup>a</sup>
	24 048.6(10)
	24 385.9(15) <sup>a</sup>
	24 488.3(12)

<sup>a</sup>Weak, see text.

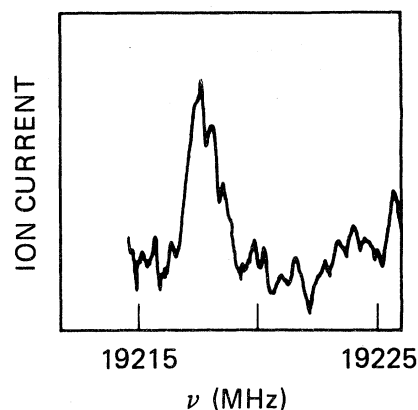


FIG. 5. A recording of a  $6s20g-6s20i$  resonance on a sweep of decreasing frequency and a relative microwave power of 0.16 as shown in Fig. 6.

sitions require only the microwave oscillator as the two-photon  $g-i$  transitions are driven by two photons of the same frequency. The three-photon  $g-k$  transitions were all driven by two microwave photons and one rf photon. However, we chose the frequencies so that the higher virtual state lay in the vicinity of the  $6sni$  state as shown in Fig. 4. Sometimes it lay below the  $6sni$  state as shown and sometimes above.

*g-h transitions.* The  $g-h$  transitions are the hardest to observe because of the small difference in the lifetimes of the  $g$  and  $h$  states. In all cases the microwave power was reduced until we reached the minimum observable linewidth  $\sim 3$  MHz, presumably due to the earth's magnetic field since no attempt was made to eliminate it. In all cases but one, we observed two transitions of equal strength (they require similar microwave powers) which are due to the splitting of the  $h$  level. For  $n=23$ , we observed four transitions, of which the two at 24 048.6 and 24 488.3 MHz are both more easily power broadened and yield larger signals. The observed frequencies are tabulated in Table I.

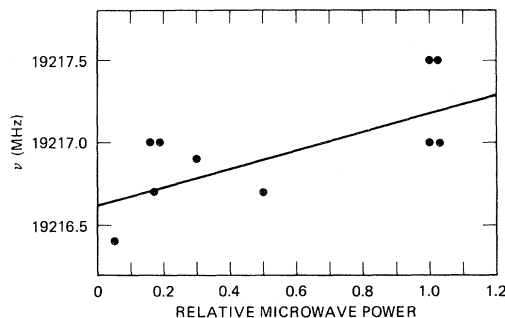


FIG. 6. The microwave power dependence of a  $6s20g-6s20i$  transition.

TABLE II. *ng-ni* intervals.

<i>n</i>	Interval (MHz)
18	51 419.6(12)
	51 658.0(12)
19	44 075.0(10)
	44 283.8(10)
20	38 433.2(10)
	38 246.2(10)
21	33 706.8(10)
	33 874.2(12)
22	30 459.2(14)
	30 607.0(9)
23	29 419.4(15)
	29 496.4(12)
	29 555.0(9)
	29 591.0(8)
	29 632.0(10)

*g-i* transitions. The *g-i* transitions are in principle easier to observe because of the greater difference in lifetimes of the *g* and *i* states, and in practice we found this to be the case. A typical resonance is shown in Fig. 5. To account for the power shifts<sup>10</sup> we observed each transition at several microwave powers and extrapolated to zero microwave power as shown in Fig. 6. As in the *g-h* transitions, for all but  $n=23$  we observed two transitions reflecting the splitting of the *ni* states. The observed *g-i* intervals, extrapolated to zero microwave power are listed in Table II. Note that the observed frequencies

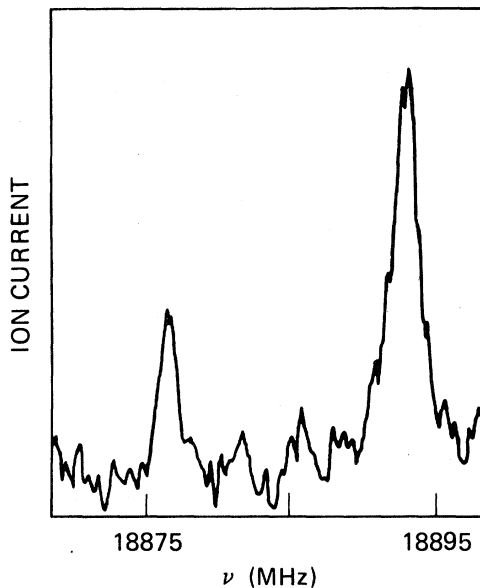


FIG. 7. A recording of the  $6s20g-6s20k$  resonance on a scan of decreasing frequency with a fixed rf frequency of 4146.5 MHz and relative rf power of 0.42.

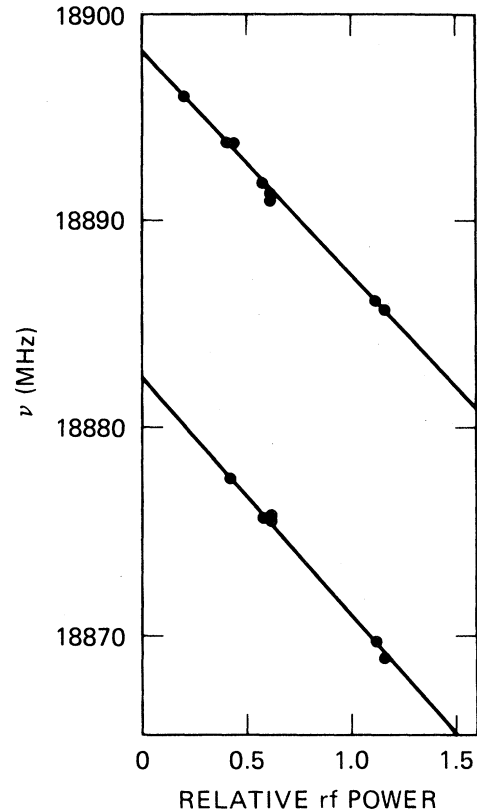


FIG. 8. The rf power shift of the  $6s20g-6s20k$  resonances for an rf frequency of 4147 MHz.

are half the listed intervals.

*g-k* transitions. The three photon *g-k* transitions were driven with two microwave photons and one rf photon, partially because this enables us to reach higher frequencies, and partially because of the fact that it is easier to produce larger microwave than rf fields in our apparatus. Since the difference in lifetimes of the *g* and *k* states is expected to be the largest of the three transitions studied it is not surprising that the observed signals are reasonably good, as shown in Fig. 7, a recording of the  $6s20g-6s20k$  resonance. It is interesting to note that in the observation of the analogous three-photon *d-h* transition in Na using a cw microwave source and fluorescence detection the long lifetime of the *h* state leads to signals much weaker than observed for the one-photon *d-f* transition.<sup>11</sup>

To verify that we were indeed observing the three-photon *g-k* transition, we varied the rf frequency over a range of  $\pm 30$  MHz and observed that the sum of the rf frequency and twice the microwave frequency was very nearly constant. Small deviations  $\sim 3$  MHz occur because of changes in the rf field strength as the frequency is changed.

TABLE III.  $ng-nk$  intervals.

$n$	Approximate rf frequency (MHz)	Approximate microwave frequency (MHz)	Interval (MHz)
18	4100	26000	56 390.2(20) 56 425.2(20)
19	3800	22000	48 328.5(23) 48 365.5(23)
20	4100	19000	41 910.8(20) 41 943.4(20)
21	3600	17000	36 885.2(23) 36 914.6(23)

The  $g-k$  transitions also exhibit power shifts due to both the microwave and rf fields. The most significant of these is the rf shift because the rf frequency is typically detuned from the  $i-k$  frequency by less than 500 MHz. In Fig. 8 we show the rf power shift of the  $6s20g-6s20k$  transitions for an rf frequency of 4147 MHz, a frequency larger than the  $6s20i-6s20j$  interval as shown in Fig. 4. If the rf frequency is set to 3246 MHz, the sign of the rf power shift is reversed as the virtual intermediate state is then above the  $6s20i$  state, unlike the levels in Fig. 4. As expected, these two cases lead to power shifts of opposite sign. The  $g-k$  intervals extrapolated to zero rf and microwave power are given in Table III. Note that again doublets of nearly equal intensity are observed from the splitting of the  $k$  states.

### C. Summary of observations

These measurements yield the  $\Delta l$  separations and the splittings of each  $l$  state. The  $\Delta l$  intervals are found to scale roughly as  $n^{-3}$  and  $l^{-5}$ , in good agreement with a dipole core polarization model.<sup>2</sup> However, a closer inspection shows that the data do not fit the usual adiabatic core polarization model and exhibit a substantial perturbation in the regularity of the  $6sng$  series. The latter is due to the presence of a perturbing  $5d7d$  state which we have located at  $41\,845.78\text{ cm}^{-1}$ . In the following sections we show that both the departure from the adi-

abatic core polarization model and the perturbation of the  $6sng$  series may be treated in the same fashion using the model of Van Vleck and Whitelaw.<sup>6</sup>

In addition to the  $\Delta l$  intervals we also are able to determine the splitting of each of the higher- (than  $l=4$ )  $l$  states to high precision. In Table IV we list the observed splittings. In Tables I–IV we have not labeled the final states explicitly since we really have no way of telling what they are. However, we can at least consider the origin of the splitting. First, recall that we saw in all cases two transitions of approximately equal strength. Thus, if the designation  $^1G_4$  of the  $6sng$  states is at all meaningful the two higher- $l$  states we observe are not likely to be singlets and triplets. This is not surprising if we recall that for the He 20g state the spin-orbit interaction and singlet-triplet (exchange) splitting are both about 1 MHz.<sup>12,13</sup> For the higher- $l$  states the effects are smaller yet with the singlet-triplet splitting decreasing faster with  $l$  than the spin-orbit splitting. When compared to the splittings in He the Ba splittings are huge, and scale as  $l^{-7}$ , faster than the approximate  $l^{-3}$  dependence expected for the spin-orbit interaction. Thus we suggest that the large splittings we see are in fact due to a spin-orbit effect, magnified by a core effect, such as the exchange core polarization which leads to huge increases in alkali-atom fine-structure intervals.<sup>14</sup>

## IV. CORE POLARIZATION

The origin of the nonadiabatic effects emerges clearly from the treatment of Van Vleck and Whitelaw so we shall outline some of the crucial points of their development.

Consider an atom with two spinless valence electrons. Its Hamiltonian is given by

$$H = \nabla_1^2 + \nabla_2^2 + f(r_1) + f(r_2) + 1/r_{12}, \quad (2)$$

TABLE IV. Intervals of the  $l > 4$  states.

$n$	$h$	$i$	$k$
18	967.4(27)	238.4(18)	35.0(35)
19	835.7(17)	208.8(15)	37.0(33)
20	680.6(13)	187.0(15)	32.6(30)
21	580.5(14)	167.4(16)	29.6(33)
22	505.3(12)	147.8(17)	
23	439.7(17)		

where  $\nabla_1^2$  and  $\nabla_2^2$  are the kinetic-energy operators,  $r_1$  and  $r_2$  are the positions of the two electrons,  $1/r_{12}$  is the Coulomb repulsion of the two electrons and  $f(r)$  is the potential due to the doubly charged core. As  $r \rightarrow \infty$ ,  $f(r) \rightarrow -2/r$ . We can expand the interaction between the two electrons in multipoles as

$$\frac{1}{r_{12}} = \frac{1}{r_>} + \frac{r_<}{r_>^2} \cos\theta_{12} + \frac{r_<^2}{2r_>^3} (3\cos^2\theta_{12} - 1) + \dots, \quad (3)$$

where  $\theta_{12}$  is the angle between  $\bar{r}_1$  and  $\bar{r}_2$ , and  $r_>$  and  $r_<$  are the larger and smaller of  $r_1$  and  $r_2$ , respectively.

Let us focus our attention on an alkaline-earth atom in which the outer electron is in a high- $n$ , high- $l$  state. For such atoms it is a reasonable approximation to say that the outer electron is always outside the inner electron. Thus if we only keep the first term of the  $1/r_{12}$  expansion, and label the two electron positions as  $r_0$  and  $r_i$  (outer and inner), in Eq. (2) there is no longer any connection between the inner and outer electrons. The solutions then are products of one-electron wave functions which satisfy the equations

$$\nabla_i^2 + f(r_i) = W_i \quad (4a)$$

and

$$\nabla_0^2 + f(r_0) + 1/r_0 = W_0. \quad (4b)$$

The energies of the states are given by the sums of the two electron energies  $W_i$  and  $W_0$  and are thus given relative to two free electrons and a doubly charged ion core. Note that Eq. (4a) corresponds to the energy levels of the singly charged ion and Eq. (4b) to the energy levels of the Rydberg electron. Recalling our previous assumption that  $r_0 > r_i$  we shall assume that  $f(r_0)$  is given by its asymptotic expression  $-2/r_0$ ; thus Eq. (4b) reduces to the equation for neutral atomic hydrogen.

At this point it is worthwhile to consider the  $\text{Ba}^+$  system of immediate interest. The first few energy levels of  $\text{Ba}^+$ , the states of the inner electron are

$$W_{d_{nl}} = \sum_{n'', n' l = l \pm 1} \frac{|\langle n'' p | \langle n' l | r_i \cos\theta_{12} / r_0^2 | 6s \rangle | nl \rangle|^2}{W_{6snl} - W_{n''pn'l}}, \quad (5)$$

where  $W_{n''pn'l}$  and  $W_{6snl}$  are the energies of the  $n''pn'l$  and  $6snl$  states. In addition the summation over  $n''$  and  $n'$  are understood to include the continua although this is not shown explicitly.

From Eq. (5) it is clear that the dependence on the inner electron comes from the matrix elements  $\langle n'' p | r_i | 6s \rangle$  and the energy separations of the  $\text{Ba}^+$  ion as shown in Fig. 9. Since the matrix element  $\langle 6p | r_i | 6s \rangle$  is more than two orders of magnitude larger than the matrix elements connecting  $6s$  to the

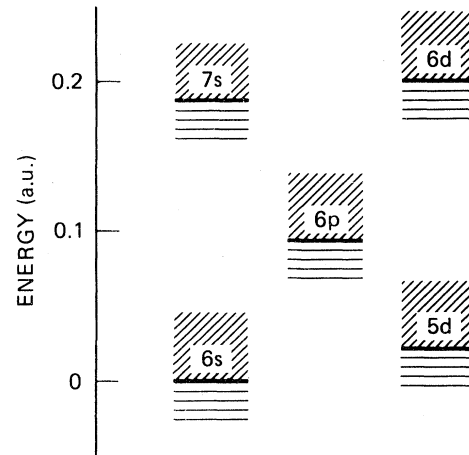


FIG. 9. Low-lying energy levels of  $\text{Ba}^+$  (—), Rydberg series of Ba (---) converging to them, and the continua (///) above each of them.

shown by the bold lines of Fig. 9, and the states of the outer electron are shown as a lighter series of lines converging to each state of  $\text{Ba}^+$ . Shaded areas above the ionic levels correspond to continua. It is to be understood that the lighter lines represent all values of  $l$  of the outer electron. Typical state vector are  $|6s\rangle |20g\rangle$  and  $|5d\rangle |20g\rangle$  which would represent the  $20g$  states converging to the  $6s$  and  $5d$  states of  $\text{Ba}^+$ . We note that the total angular momentum  $L$ , is equal to four for the  $|6s\rangle |20g\rangle$  state but may be anywhere from two to six for the  $|5d\rangle |20g\rangle$  state. (Recall that we have assumed spinless electrons.) Since we are only considering interactions within the atom the total angular momentum  $L$  is conserved and only states of the same  $L$  interact. Although we shall not write  $L$  or its projection  $M$  on the axis of quantization explicitly we must remember that they do not change.

In this approximation the states  $6s20l$  are all degenerate, however the degeneracy is removed by including the higher-multipole terms in the  $1/r_{12}$  expansion of Eq. (3). If we confine our attention to the  $6snl$  states it is clear that the second term on the right-hand side of Eq. (3) leads, by second-order perturbation theory, to a shift  $W_{d_{nl}}$  given by

higher- $p$  states we omit all the  $n''p$  terms in Eq. (5) other than  $6p$ . Thus it is not necessary to sum over  $n''$ . The angular part of Eq. (5) (or of the analogous higher-multipole terms) may be reduced using either the approach of Van Vleck and Whitelaw or that of Edmonds.<sup>15</sup> The latter consists of evaluating the scalar product of spherical harmonics for the inner and outer electrons. This leads to

$$W_{d_{nl}} = \frac{|\langle 6p | r | 6s \rangle|^2}{3} \left[ \sum_{n'} \frac{l |\langle n'l-1 | 1/r_0^2 | nl \rangle|^2}{(2l+1)(W_{6s_{nl}} - W_{6p_{n'l-1}})} + \sum_{n'} \frac{(l+1) |\langle n'l+1 | 1/r_0^2 | nl \rangle|^2}{(2l+1)(W_{6s_{nl}} - W_{6p_{n'l+1}})} \right]. \quad (6)$$

If the spread in energies of the  $n'l'$  ( $l'=l\pm 1$ ) states involved in the sums of Eq. (6) is small compared to the ion separation  $W_{6p} - W_{6s}$ , then we may approximate  $W_{6p_{n'l\pm 1}} - W_{6s_{nl}}$  by the ionic separation and remove it from the sum. This yields finally

$$W_{d_{nl}} = - \frac{|\langle 6p | r_i | 6s \rangle|^2}{3(W_{6p} - W_{6s})} \left[ \frac{l}{2l+1} \sum_{n'} |\langle n'l-1 | 1/r_0^2 | nl \rangle|^2 + \frac{l+1}{2l+1} \sum_{n'} |\langle n'l+1 | 1/r_0^2 | nl \rangle|^2 \right]. \quad (7)$$

Note that

$$|\langle 6p | r_i | 6s \rangle|^2 / 3(W_{6p} - W_{6s})$$

is twice the dipole polarizability of the  $Ba^+ 6s$  state. Van Vleck<sup>16</sup> has shown that

$$\langle nl | r^{2s} | nl \rangle = \sum_{n'} |\langle n'l' | r^s | nl \rangle|^2 \quad (8)$$

for any value of  $l'$ . Thus Eq. (7) may be rewritten as

$$W_{d_{nl}} = - \frac{\alpha_d}{2} \langle nl | 1/r_0^4 | nl \rangle \quad (9)$$

which is the first term of Eq. (1). Here  $r_0$  corresponds to  $r$  in Eq. (1).

From the preceding development it is clear that the nonadiabatic effects arise from the fact that in general  $W_{6p_{n'l'}} - W_{6s_{nl}} \neq W_{6p} - W_{6s}$ . Thus it is the energy distribution of the matrix elements  $\langle n'l' | 1/r_0^2 | nl \rangle$  which leads to the nonadiabatic effects, and the magnitude of the nonadiabatic effects will be determined by the spread in energies of  $\langle n'l' | 1/r_0^2 | nl \rangle$  relative to the energy of the ionic transition.

To provide a feeling for the energy spreads, the values of  $|\langle n'l\pm 1 | 1/r^2 | nl \rangle|^2$  are shown in Fig. 10 for  $n=18$  and  $l=5$ , the  $6s18h$  state. The values shown are calculated by numerical integration using hydrogenic wave functions, which give physically meaningful behavior for  $r \rightarrow 0$ . In previous numerical calculations<sup>17,18</sup> involving bound Coulomb wave functions transformations allowing a grid size which increases with  $r$  have been used to match the increasing period of oscillation of the wave function as  $r$  is increased. However, for continuum waves, the period of the wave function's oscillations does not increase appreciably for  $r > 1/E$  where  $E$  is the energy of the continuum state. Thus, we have used a constant grid size  $\sim 1a_0$  in the numerical integra-

tions.

The values shown in Fig. 10 are normalized per unit energy (each bound-state value is multiplied by  $n'^3$  and given an energy width of  $n'^{-3}$  as is done by Fano and Cooper<sup>19</sup>). Thus, according to Eq. (8), the area under each curve should be equal to  $\langle 18h | 1/r^4 | 18h \rangle$ . In fact we find this to be true to better than 1%, confirming the numerical accuracy of the calculations. As can be seen from Fig. 10, the values of  $|\langle n'l-1 | 1/r^2 | nl \rangle|^2$  lie below the  $Ba^+ 6p$  limit and the values for  $|\langle n'l+1 | 1/r^2 | nl \rangle|^2$  lie above the  $Ba^+ 6p$  limit. Not surprisingly the energy spread of the matrix elements is considerably greater for  $l=5$  than for  $l=7$  (not shown here), and correspondingly the

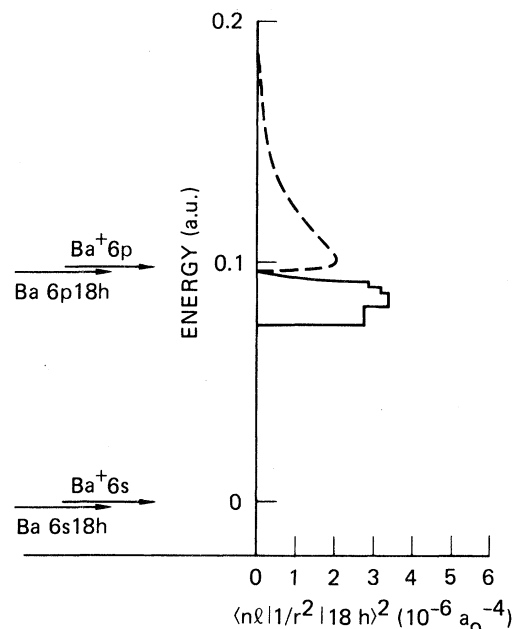


FIG. 10. The squared matrix elements  $\langle ng | 1/r^2 | 18h \rangle^2$  (—) and  $\langle ni | 1/r^2 | 18h \rangle^2$  (---) plotted vs energy to show the energy distribution of the matrix elements.

nonadiabatic effects are larger. Finally, the shape of the analogous  $|\langle n'l \pm 1 | 1/r^2 | 23l \rangle|^2$  curves are identical, within a scale factor, to the  $n = 18$  curves typified by Fig. 10.

It is useful to connect the results of the presumably accurate expression Eq. (7) with the adiabatic polarization formula Eqs. (1) and (9) by defining the factor  $k_d$ ,

$$k_d \langle nl | 1/r^4 | nl \rangle = (W_{6p} - W_{6s}) \left[ \frac{l}{2l+1} \sum_{n'} \frac{|\langle n'l-1 | 1/r^2 | nl \rangle|^2}{W_{6pn'l-1} - W_{6snl}} + \frac{l+1}{2l+1} \sum_{n'} \frac{|\langle n'l+1 | 1/r^2 | nl \rangle|^2}{W_{6pn'l+1} - W_{6snl}} \right]. \quad (10)$$

The values we have calculated for  $k_d$  are listed in Table V. We find, not unexpectedly, negligible variation with  $n$  over the range  $18 \leq n \leq 23$ .

The next term in the expansion of  $1/r_{12}$ , the quadrupole term equal to  $(r_i^2/2r_0^3)(3\cos^2\theta_{12}-1)$ , may be treated in exactly the same manner. The only difference is that  $6snl$  states are coupled to  $n'dn'l'$  states where  $l' = l-2, l, l+2$ . If we assume that only the low-lying  $5d$  state of  $Ba^+$  shown in Fig. 9 leads to an appreciable energy shift, the energy shift is given by<sup>6</sup>

$$\Delta W_{qnl} = \langle 5d | r_i^2 | 6s \rangle^2 \left[ \frac{3}{10(4l^2-1)(2l+3)} \left( (2l-1)(l+1)(l+2) \sum_{n'} \frac{|\langle n'l+2 | 1/r_0^3 | nl \rangle|^2}{W_{6snl} - W_{5dn'l+2}} + \frac{2(l^2+l)(2l+1)}{3} \sum_{n'} \frac{|\langle n'l | 1/r_0^3 | nl \rangle|^2}{W_{6snl} - W_{5dnl}} + (2l+3)(l^2-l) \sum_{n'} \frac{|\langle n'l-2 | 1/r_0^3 | nl \rangle|^2}{W_{6snl} - W_{5dn'l-2}} \right) \right]. \quad (11)$$

We estimate that ignoring the higher- $d$  states of  $Ba^+$  leads to an error  $\sim 10\%$ . To a first approximation the numerical weightings of the  $|\langle n'l' | 1/r_0^3 | nl \rangle|^2$  sums are given by the ratio 3:2:3 for  $l' = l+2, l, l-2$ .

If the energy distributions of the  $|\langle n'l' | 1/r_0^3 | nl \rangle|^2$  matrix elements cover a small range compared to the ionic  $6s$ - $5d$  separation the energy denominators may be taken out of the summations, and each summation, by Eq. (8), reduces to  $\langle nl | 1/r^6 | nl \rangle$ . Thus Eq. (11) reduces to

$$\Delta W_{qnl} = -\frac{1}{5} \frac{\langle 6s | r_i^2 | 5d \rangle^2}{W_{5d} - W_{6s}} \langle nl | 1/r_0^6 | nl \rangle. \quad (12)$$

With

$$\alpha_q = \frac{2}{5} \frac{|\langle 6s | r_i^2 | 5d \rangle|^2}{W_{5d} - W_{6s}}, \quad (13)$$

Eq. (12) reduces to the quadrupole part of Eq. (1).

As for the dipole interaction the range of energies covered by  $|\langle n'l' | 1/r_0^3 | nl \rangle|^2$  determines the

TABLE V. Calculated values of  $k_d$ .

$l=4$	$l=5$	$l=6$	$l=7$
0.945	0.953	0.965	0.975

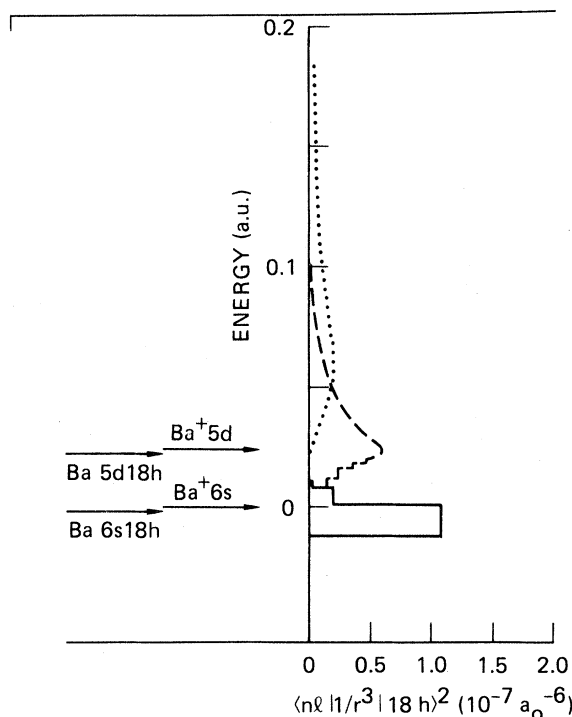


FIG. 11. The squared matrix elements  $\langle nf | 1/r^3 | 18h \rangle^2$  (—),  $\langle nh | 1/r^3 | 18h \rangle^2$  (---), and  $\langle nk | 1/r^3 | 18h \rangle^2$  (····) plotted vs energy to show the energy distribution of the matrix elements. Note that most of  $\langle nf | 1/r^3 | 18h \rangle^2$  lies below the  $6s18h$  state.

magnitude of the nonadiabatic effects. For  $l'=l-2, l$ , and  $l+2$  the major contributions to  $|\langle n'l' | 1/r_0^3 | 6snl \rangle|^2$  comes from the lowest-lying  $5dn'l'$  states,  $n' = \infty$  (the vicinity of the  $\text{Ba}^+ 5d$  limit), and above the  $\text{Ba}^+ 5d$  ionization limit, respectively.

This is shown in Fig. 11 for the  $n=18, l=5, 6s18h$  states. It is clear that, much more so than for the dipole terms, it is a poor approximation to use  $W_{5dn'l'} - W_{6snl} = W_{5d} - W_{6s}$ . From Fig. 11 it is evident that the effect of  $5dn'l+2$  states is tremendously reduced by the vastly increased energy denominator. Since the  $|\langle n'l | 1/r_0^3 | nl \rangle|^2$  values are centered near the  $\text{Ba}^+ 5d$  ionization limit the nonadiabatic effects are not so severe. However the  $|\langle n'l-2 | 1/r_0^3 | nl \rangle|^2$  matrix elements states are weighted to very low  $n'$  with the result that the effect of these states is greatly enhanced due to the diminished energy denominators. Note that the lowest-lying  $l-2$  state has the largest matrix element. As shown by Fig. 11 for the  $l=5$  state the sign of the energy denominator is in fact reversed since the  $5d4f$  level lies below the  $6snh$  level.

We again make connection with the adiabatic polarization formula by defining  $k_q$ , analogous to  $k_d$ ,

$$k_q \langle nl | 1/r_0^6 | nl \rangle = -5\chi(W_{5d} - W_{6s}), \quad (14)$$

where  $\chi$  is defined implicitly using Eq. (11) as  $\Delta W_{qnl} = \langle 5d | r_i^2 | 6s \rangle^2 \chi$ . We have calculated  $k_q$  using hydrogenic wave functions of the  $l=5, 6$ , and  $7$  states  $n=18$  and  $23$  with the results shown in Table VI. For the  $5dnf$  states we used hydrogenic wave functions, which have physically realistic behavior for small  $r$ , but used a quantum defect of  $0.2$  to more accurately represent the energies of the  $f$  states. The variation, which is largest for the  $l=5$  states, is due to the variation in the energy denominators  $W_{5dn'l-2} - W_{6snl}$  as  $n$  is changed. By using our computed values of  $k_d$  and  $k_q$  we can represent the polarization energy as

$$\Delta W_{\text{pol}} = -\frac{\alpha_d k_d \langle 1/r^4 \rangle}{2} - \frac{\alpha_q k_q \langle 1/r^6 \rangle}{2}. \quad (15)$$

We note that if one of the  $5dn'l-2$  states is very close to a  $6snl$  state a substantial perturbation occurs which is not accurately treated in this way

TABLE VI. Calculated values of  $k_q$ .

$n$	$l=5$	$l=6$	$l=7$
18	-0.430	1.67	1.11
23	-0.355	1.89	1.13

since we have ignored all effects of spin (and exchange), and real Ba atoms have two spinning valence electrons. If we sum over all the states, their exact energy distribution (spin orbit, exchange splittings) does not matter. However, if one state creates a local perturbation, we must know how to represent it accurately. It is for this reason that the perturbed  $6sng$  states are not included in Table VI.

## V. POLARIZATION ANALYSIS OF THE DATA

Edlen<sup>2</sup> has defined the terms  $P$  and  $Q$ ,  $P = R \langle 1/r^4 \rangle$  and  $Q = \langle 1/r^6 \rangle / \langle 1/r^4 \rangle$  where  $R$  is the Rydberg constant in  $\text{cm}^{-1}$  which enables us to write Eq. (1) as

$$W_{\text{pol}} = -\alpha_d P - \alpha_q PQ, \quad (16)$$

where  $W_{\text{pol}}$  is given in  $\text{cm}^{-1}$  (in the notation of Ref. 5,  $\Delta p = \alpha_d P + \alpha_q PQ$ ). Since we measure the intervals between  $l$  states not their depressions below the hydrogenic level, we use the approach of Safinya *et al.*<sup>5</sup> to rewrite Eq. (16) as

$$\frac{\Delta W_{\text{pol}}}{\Delta P} = \frac{W_{\text{pol}l} - W_{\text{pol}l'}}{\Delta P} = \alpha_d + \frac{\alpha_q \Delta PQ}{\Delta P}, \quad (17)$$

where  $\Delta P = P_l - P_{l'}$  and  $\Delta PQ = P_l Q_l - P_{l'} Q_{l'}$ . Dividing Eq. (16) by  $\Delta P$  divides the dominant dipole part of the polarization energy out of both sides of the equation.

Thus, if we use the experimentally measured values for  $\Delta W_{\text{pol}}$  (in  $\text{cm}^{-1}$ ) and plot the values of  $\Delta W_{\text{pol}}/\Delta P$  vs  $\Delta PQ/\Delta P$ , we should find a graph of slope  $\alpha_q$  and intercept  $\alpha_d$ . Doing this for our Ba

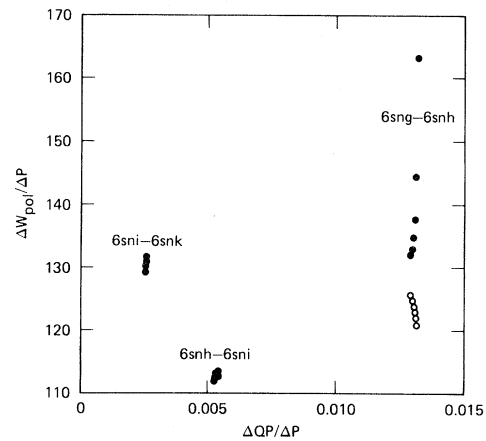


FIG. 12. A plot of the measured  $\Delta l$  intervals using the adiabatic core polarization model. From the uncorrected intervals ( $\bullet$ ) with the  $6sng-6snh$  intervals corrected for the evident perturbation ( $\circ$ ) at  $n=5$ .

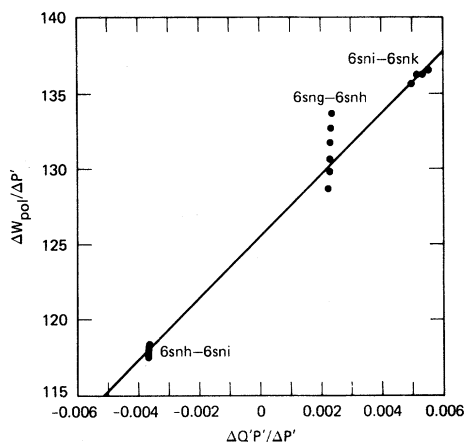


FIG. 13. A plot of the measured  $\Delta l$  intervals using the factors  $k_d$  and  $k_q$  to correct for the nonadiabatic effects. The  $6sng-6snh$  frequencies have been corrected to remove the strong perturbation.

data, using the average of the two  $6sng-6sni$  intervals to determine the center of the interval, yields the graph of Fig. 12. Even if we ignore the transitions involving  $6sng$  states which are clearly perturbed, we find an apparently negative value of  $\alpha_q$  which is physically impossible.

If we plot our data, using the correction factors  $k_d$  and  $k_q$  to account for the nonadiabatic effects the data look much more reasonable. Explicitly, we use  $P' = k_d P$  and  $Q' = k_q Q$ . This leads to the results shown in Fig. 13, the data for the  $6snh-6sni$  and  $6sni-6snk$  intervals plotted using  $P'$  and  $Q'$  in place of  $P$  and  $Q$ .

In principle we could include the  $6sng-6snh$  data in Fig. 13 using only the correction factors  $k_d$  and  $k_q$ . The drastic perturbation of the  $6sng-6snh$  frequencies clearly comes from a quadrupole interaction with a specific  $5dnd$  state perturbing the  $6sng$  series, and this should be manifested as a rapid variation in  $k_q$  with  $n$ . However, as noted above, the actual perturbing state has some presently unknown combination of spins of the two electrons and is not accurately represented by our calculations which assumes spinless electrons. The actual  $1/r_0^3$  magnitude of the matrix element is thus not equal to the value we would calculate using our spinless model. The simplest way to account for this is to note that the energy shift of a  $6sng$  state due to the  $5dnd$  state which we take to be the  $5d7d$  state is given by

$$\Delta_{5d7d} = \beta \frac{|\langle 5d | r_i^2 | 6s \rangle|^2}{W_{6sng} - W_{5d7d}} |\langle 7d | 1/r_0^3 | ng \rangle|^2, \quad (18)$$

where  $\beta$  is a constant of order one. The matrix ele-

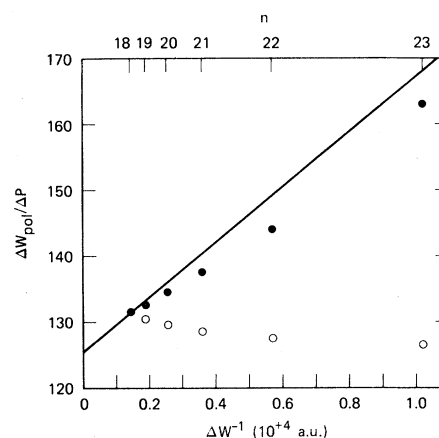


FIG. 14. A plot of  $\Delta W_{\text{pol}}/\Delta P$  vs  $\Delta W^{-1}$ , the inverse of the energy to the perturbing state at  $41845.78 \text{ cm}^{-1}$  (●). The observed dependence may be decomposed into a part which depends linearly on  $n$  (○) and a part which depends linearly on  $\Delta W^{-1}$  (—). This enables us to remove the effect of the local perturbation near  $41845.78 \text{ cm}^{-1}$  from our data.

ment  $|\langle 7d | 1/r_0^3 | ng \rangle|^2$  scales as  $n^{-3}$  and the inverse of the resonance denominator. In the absence of a nearby perturber, the quantity  $\Delta W_{\text{pol}}/\Delta P$  would exhibit a linear variation in  $n$ , the sign depending upon the value of  $k_q$ . The variation due to  $\Delta_{5d7d}$  scales as the inverse of the energy difference from the perturber. Our preliminary measurements show the perturber at  $41845.78 \text{ cm}^{-1}$ . In Fig. 14 we show a plot of  $(W_{nh} - W_{ng})/\Delta P$  vs the inverse of the energy separation  $\Delta W^{-1}$  from the perturber. Assuming that the variation of Fig. 14 is due to a linear dependence on  $n$  plus a linear dependence on the inverse energy separation  $\Delta W^{-1}$  we can remove the effect due to  $\Delta_{5d7d}$ , with the results shown in Fig. 14 for  $(W_{nh} - W_{ng})/\Delta P$ .

Since we have removed the interaction with the  $5d7d$  state from the experimental data, we should do likewise in calculating  $k_q$ . Doing this by omitting the contribution from the  $5dnd$  state just below the  $\text{Ba}^+ 6s$  limit we find that for the  $l=4$  states  $k_q = 0.117$ . Using this value of  $k_q$  and the value of  $k_d$  from Table V, we have plotted the  $6sng-6snh$  data on Fig. 13 and they are certainly consistent with the  $6snh-6sni$  and  $6sni-6snk$  data. Since it is now apparent that the extreme variation of the  $g-h$  interval is due to the perturbing  $5d7d$  level it is only fair to apply the correction of Fig. 14 to the  $6sng-6snh$  data in Fig. 12. Our doing this results in the open circles of Fig. 12 which hardly help in determining a slope and an intercept  $\alpha_q$  and  $\alpha_d$ .

From Fig. 13 we derive the values

$$\alpha_d = 125.5(10)a_0^3,$$

$$\alpha_q = 2050(100)a_0^5$$

for the dipole and quadrupole polarizability of the  $Ba^+ 6s$  state. These values are in reasonably good agreement with the values we have calculated using the Coulomb approximation and the method of Zimmerman *et al.*,<sup>17</sup>

$$\alpha_d = 122.6a_0^3,$$

$$\alpha_q = 2589a_0^5.$$

This value of  $\alpha_q$  is calculated considering only the  $5d$  state of  $Ba^+$ . The inclusion of higher  $nd$  states raises the value of  $\alpha_q$  by 10%.

Thus it appears that the method of Van Vleck and Whitelaw which is based on a very simple no-

tion may be used to determine with reasonable accuracy the nonadiabatic effects in the core polarization model. Furthermore this approach makes completely apparent the connection between configuration interaction and core polarization which is not so apparent using the adiabatic core polarization model.

#### ACKNOWLEDGMENTS

This work was supported by the National Science Foundation under Grant No. PHY-8007041. We are pleased to acknowledge the generous loan of microwave equipment by J. Watgen and useful discussions with A. P. Hickman, R. P. Saxon, D. L. Huestis, and W. E. Cooke.

- 
- <sup>1</sup>J. E. Mayer and M. G. Mayer, *Phys. Rev.* **43**, 605 (1933).  
<sup>2</sup>B. Edlen, in *Handbuch der Physik* (Springer, Berlin, 1964), Vol. 27.  
<sup>3</sup>R. R. Freeman and D. Kleppner, *Phys. Rev. A* **14**, 1614 (1976).  
<sup>4</sup>W. E. Cooke, T. F. Gallagher, R. M. Hill, and S. A. Edelstein, *Phys. Rev. A* **16**, 2473 (1977).  
<sup>5</sup>K. A. Safinya, T. F. Gallagher, and W. Sandner, *Phys. Rev. A* **22**, 2672 (1980).  
<sup>6</sup>J. H. Van Vleck and N. G. Whitelaw, *Phys. Rev.* **44**, 551 (1933).  
<sup>7</sup>A. G. Vaidyanathan and P. Shorer, *Bull. Am. Phys. Soc.* **26**, 1317 (1981).  
<sup>8</sup>W. E. Cooke, T. F. Gallagher, R. M. Hill, and S. A. Edelstein, *Phys. Rev.* **21**, 588 (1980).  
<sup>9</sup>J. A. Armstrong, J. J. Wynne, and P. Escherick, *J. Opt. Soc. Am.* **69**, 211 (1979).  
<sup>10</sup>S. H. Autler and C. H. Townes, *Phys. Rev.* **100**, 703 (1955).

- <sup>11</sup>T. F. Gallagher, R. M. Hill, and S. A. Edelstein, *Phys. Rev. A* **14**, 744 (1976).  
<sup>12</sup>J. W. Farley, K. B. MacAdam, and W. H. Wing, *Phys. Rev. A* **20**, 1754 (1979).  
<sup>13</sup>H. A. Bethe and E. A. Salpeter, *Quantum Mechanics of One and Two Electron Atoms* (Academic, New York, 1957).  
<sup>14</sup>R. M. Sternheimer, J. E. Rodgers, T. Lee, and T. P. Das, *Phys. Rev. A* **14**, 1595 (1976).  
<sup>15</sup>A. R. Edmonds, *Angular Momentum in Quantum Mechanics* (Princeton University, Princeton, N. J., 1960).  
<sup>16</sup>J. H. Van Vleck, *Proc. Nat. Acad. Sci.* **15**, 757 (1929).  
<sup>17</sup>M. L. Zimmerman, M. G. Littman, M. M. Kash, and D. Kleppner, *Phys. Rev. A* **20**, 2251 (1979).  
<sup>18</sup>S. A. Bhatti, C. L. Cromer, and W. E. Cooke, *Phys. Rev. A* **24**, 161 (1981).  
<sup>19</sup>U. Fano and J. W. Cooper, *Rev. Mod. Phys.* **40**, 441 (1968).